*metals*

MDPI

*Article*

# Influence of Different Filler Metals on the Mechanical and Microstructural Characteristics of Arc-Welded Joints Made of Dissimilar Titanium Alloys

**Silvia Gaiani [1,*], Marica Gozzi [2], Elisa Ferrari [2], Alberto Menozzi [2], Magdalena Lassinantti Gualtieri [3], Elena Colombini [3] and Paolo Veronesi [3,*]**

[1] V System s.r.l., 41042 Fiorano Modenese, Italy
[2] Veca S.p.A., 41019 Soliera, Italy
[3] Engineering Department "Enzo Ferrari", University of Modena and Reggio Emilia, 41125 Modena, Italy
* Correspondence: silvia.gaiani@vsystem.it (S.G.); paolo.veronesi@unimore.it (P.V.)

**Abstract:** In the motorsport industry, the choice of material for manufacturing the heat resistant components often falls on titanium alloys. In most cases, the production flow for this kind of part involves CNC machining and subsequent assembly by welding process, to other parts obtained by cold plastic forming and possibly made using different titanium alloys. Hence, the alloying element-content in the joint area can be extremely heterogeneous and variable point-by-point. To investigate this topic further, dissimilar welding of the alpha/beta alloy Ti6Al4V and of the oxidation-resistant alpha alloy KS-Ti 1.2 ASN-EX was made by GTAW technology and using different filler metals. Chemical and mechanical properties of the welds were investigated by XRD, SEM-EDS, microhardness maps, and tensile and bending tests. Results show that, despite the different alloying elements present in the two filler wires investigated, static properties of the welds are similar. Results also show that the local V/Al content ratio affects the microhardness as it is responsible for the creation of supersaturated alpha phases during the cooling of the weld beads.

**Keywords:** GTAW welding; titanium alloys; filler metal; dissimilar welds



**Citation:** Gaiani, S.; Gozzi, M.; Ferrari, E.; Menozzi, A.; Lassinantti Gualtieri, M.; Colombini, E.; Veronesi, P. Influence of Different Filler Metals on the Mechanical and Microstructural Characteristics of Arc-Welded Joints Made of Dissimilar Titanium Alloys. *Metals* **2023**, *13*, 1482. https://doi.org/10.3390/met13081482

Academic Editor: António Bastos Pereira

Received: 14 July 2023
Revised: 11 August 2023
Accepted: 16 August 2023
Published: 18 August 2023



## 1. Introduction

For the manufacture of the heat resistant components used for aerospace and motorsport applications, it is a common practice to require the joining together of different titanium alloys displaying different microstructures. In general, for welding dissimilar materials, the potential issues for attaining good joints are ascribable to differences in melting temperature and thermal expansion coefficients of the two materials, which may lead to higher thermal stresses and result in cracking in the transition zone between the materials [1]. Hence, challenges in joining an α + β titanium alloy to an α Ti one are mainly represented by the mismatch in mechanical properties, melting temperatures in the case when a molten phase is involved, crystal structures, and, perhaps more importantly, mutual solubility.

Two of the most common joining techniques in the aerospace sector are electron beam welding (EBW) and linear friction welding (LFW). However, both techniques induce a significant level of residual stress in the assembled part, resulting in premature failure and reduction in the fatigue life in presence of surface residual tensile stresses [2,3].

Among possible joining techniques, solid state welding has gained an increasing importance and it has been qualified also by the aerospace sector because the welds are practically free from defects such as porosity or inclusions, and the resulting microstructure presents fine grains in the central joining zone with limited thermomechanically-affected zones and heat-affected zones (HAZ) [4]. In the past, solid state joining by inertia-friction, linear-friction, and friction-stir welding have been used, demonstrating some relevant

benefits with respect to arc welding due to short joining time, direct heat input at the weld interface, and a relatively thin heat-affected zone [5].

The basic form of the friction stir welding process uses a cylindrical (non-consumable) tool, consisting of a flat circular shoulder, with a smaller probe protruding from its center. The tool rotates and it is forced into the joint line (usually the line between two rigidly clamped plates) so that the probe is buried in the workpiece, while the shoulder lies on the surface of the parts to be joined. Heat is generated by the friction between the rotating tool and the plate material, while pressure is applied, resulting in a plasticized zone formed around the probe. The tool moves, and stirs the plasticized area, frictionally heating and plasticizing new material along the joint line [6]. Being a generally melt-free technique, friction stir welding can enable a better control over the grain size. However, the peak temperature at and near the joint interface can be very high and lead to the formation of brittle intermetallic compounds or other defects, resulting in non-uniformity in the flow pattern, composition, and microstructure, especially if the beta transus temperature is surpassed [7]. In the case of titanium, friction stir welding requires particular care due to titanium alloys low thermal conductivity. Therefore, the main heat generated around tool shoulder is difficult to transfer downwards during welding, leading to a large temperature gradient along the thickness. As a result, the achievement of a defect-free joint is generally constrained within a quite narrow process window [8]. Due to the low thermal conductivity of such an alloy, it is difficult to remove heat from the welding zone, and the use of an active liquid cooling system could be required [9]. Moreover, the high tendency of titanium alloys to oxidation at high temperature requires the use of protection in the form of inert gas (usually argon) in the contact zone between the tool and the material [10]. Last but not least, the tools used for friction stir welding of titanium should present a high tribological friction resistance when paired with titanium. Tool and titanium alloy contact at high temperatures can also lead to more complex interactions, such as mutual diffusion dissolution of the tool and material, formation of secondary phases on the tool surface, formation of the tribological layer and its destruction, and mixing of fragments into the material of the joint or processing zone [11].

Another relevant technique to join dissimilar materials, and titanium alloys too, is diffusion bonding. The diffusion bonding can occur as either a solid-state or a liquid-phase bonding process. The solid-state variant involves heating of the surfaces to be joined to a temperature which is typically in the range of 60–80% of the melting point temperature of the lowest melting point base metal or interlayer. The first step of the process involves contact of the surfaces to be joined, leading to a local deformation of the surface asperities under the effects of heat and static pressure. This is followed by heating and holding the parts to be joined at the bonding temperature to have inter-diffusion to take place. Parameters of importance in solid-state bonding are bonding time, contact pressure, bonding temperature, surface roughness, and interlayer composition [12].

The strength of solid-state diffusion bond can be improved by optimizing the bonding temperature, bonding pressure, and bonding time, and via post-bonded heat treatments. Moreover, the use of interlayers was also shown to be effective in achieving sound diffusion bond [13]. However, interdiffusion occurring between the interlayer and base materials can result in possible anomalies such as porosity or intermetallic formation [12].

Reducing the diffusion bonding time can help decreasing the occurrence of such defects, for instance using Field Assisted Sintering Techniques (FAST). In a recent paper [13], three different combinations of dissimilar titanium alloys were bonded including metastable beta, alpha-beta, and alpha titanium alloys; FAST-diffusion bonded with a dwell temperature of 1200 °C and a pressure of 35 MPa. The hardness profiles revealed a hard phase at the interface for alloy combinations containing the metastable beta alloy.

However, conventional diffusion bonding has some practical limits, namely, the size limitation of the furnace chamber and the uniformity of the pressure applied across the entire surface area of the part. Run times are also long, compared to other techniques.

Moreover, large format parts of low thickness are difficult to join with a reproducible deformation [14].

Long before solid state welding or diffusion welding came into existence, fusion welding had, and still has, an innate ability to join the structures with complicated geometries. GTAW (Gas Tungsten Arc Welding) is based on the creation of a weld bonding by making an electric arc with a non-consumable tungsten electrode and protecting the molten pool through a protective gas stream. Due to the generally low deposition rate of this technique, filler metal can be used as well, added manually or mechanically to the weld area [15].

GTAW technology, performed in manual mode, is widely used in the motorsport segment to weld components made of titanium alloy [16]. This technique has been known for a long time, and in most cases, the joints are made in special inert gloveboxes in order to prevent the well-known oxidation problems in the weld bead and HAZ adjacent areas [15]. GTAW welding requires careful positioning of the edges but may allow, if properly performed, the achievement of high-quality joints displaying good mechanical strength [17]. The formation of intermetallic phases in the weld and the contaminations imparted by the filler materials are the primary downsides of fusion welding.

In this framework, arc welding, despite the formation of a liquid phase, also has the potential to process large parts and reduced thickness of the base materials. However, during the welding of titanium alloys, high fusion temperature, combined with low thermal conductivity, may result in a steep temperature gradient in the adjacent areas to the weld beads (WB), leading to multiple phase transformations in the heat effected zone (HAZ) [18]. Due to this, it is expected that the microstructure from WB to the base material (BM) of the weldment is formed in a heterogeneous mode.

The HAZ undergoes both rapid heating and cooling that, in the case of (α + β) alloys, cause significant growth of the prior-β grains [19]. The microstructure of the WB results from the combination of solidification and solid-state transformation processes, resulting in coarse prior-β grains and acicular α and ά phases, the latter being typical of higher cooling rates such as the ones occurring with electron beam welding. Consequently, a decrease in ductility and of mechanical properties was often recorded in Ti6Al4V TGAW welds due to their coarse-grained microstructure [20].

Understanding the correct welding parameters, and also the most appropriate filler metal, which may lead to have a better homogeneity in the weld zone, is a crucial aspect, and also has the aim to better predict the final joint performance and prevent defect formation during the solidification of the molten pool. Especially in the case of welds of dissimilar alloys, identifying the right filler material that allows obtaining a joint that meets all the quality requirements imposed by the customer's specifications becomes a strategic factor.

In our specific case, and subject of this study, a further critical issue lies in the fact that one of the two base materials in this study, namely, the α-type alloy called KS-Ti 1.2 ASN-EX, is not unified according to current international standards and is, in fact, a proprietary alloy of the Japanese manufacturer Kobe Steel ltd. Unfortunately, there are no standard filler wires of this material and, therefore, in order to qualify the process according to ISO 15614-1, it is necessary to test and identify unified filler materials according to AWS and EN standards. Based on this assumption, two different potentially suitable filler materials were identified for this study:

- ER Ti-5: wire presenting the chemical composition of Ti6Al4V alloy (Grade 5) belonging to the family with α + ß microstructure;
- ER Ti 9: wire presenting the chemical composition of Ti3Al2V alloy (Grade 9) belonging to the family with near-α microstructure. This alloy exhibits the same ligands as the previous one but with half the percentages.

The novelty of this work lies in the use of a rather conventional and high throughput technique, such as GTAW, to join thin sheets of dissimilar alpha and alpha-beta titanium alloys, for which no standard filler metal is prescribed. The aim is to identify the most suitable filler material, among the ones presenting compositional similarities with one

of the two base metals, able to maximize chemical and structural homogeneity to have heterogeneous welded joints with no external defects.

## 2. Materials and Methods

### *2.1. Samples*

For the present study, nr. 5 butt joints realized on pipes welded in an overhead welding position (6G) were made for each type of combinations of the base material and filler metal investigated. The welding configuration is depicted in Figure 1.

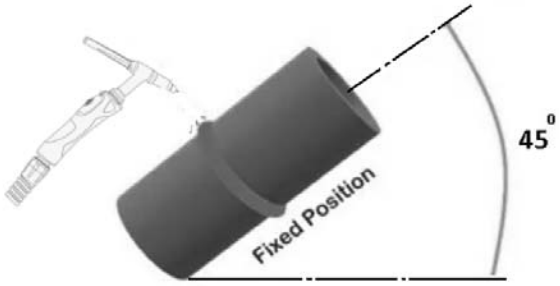


**Figure 1.** 6G overhead welding position.

The effective chemical composition of the materials used in the present study, as declared by the suppliers, is shown in Table 1.

**Table 1.** Chemical composition of base materials and filler metals (wt%).

| Material | Al (%) | V (%) | Si (%) | Nb (%) | C (%) | Fe (%) | O (%) | H (%) | N (%) | Ti |
|---|---|---|---|---|---|---|---|---|---|---|
| Ti6Al4V | 6.30 | 4.31 | -- | -- | 0.010 | 0.010 | 0.112 | 0.004 | 0.011 | Bal. |
| Ti-KS 1.2ASN-EX | 0.53 | -- | 0.41 | 0.21 | 0.032 | 0.113 | 0.098 | 0.007 | 0.013 | Bal. |
| ER Ti-5 | 6.28 | 4.14 | -- | -- | 0.024 | 0.157 | 0.130 | -- | 0.008 | Bal. |
| ER Ti-9 | 3.04 | 2.50 | -- | -- | 0.010 | 0.187 | 0.074 | 0.002 | 0.003 | Bal. |

The base metal was originally supplied in sheet form with 1 mm thickness, and subsequently hand rolled for shaping the pipes used for the characterization. The pipes were welded longitudinally using a semi-automatic linear seam welder with a direct current electrode negative (DCEN) of 28 A and a travelling speed of 8 mm/s.

The delivery conditions of the materials were:

- Annealed, for $\alpha$ alloy Ti-KS 1.2 ASN-EX;
- Solution treated for $\alpha + \beta$ alloy Ti6Al4V.

Annealing of ASN-EX samples was performed by Kobe Steel, processing two coils at the time in a vacuum furnace held at 780 °C for 24 h.

The two different filler materials used for the trials, namely, rods having 1.16 mm diameter, were produced according to AWS A5.16 standard [21].

Table 2 summarizes the materials combinations investigated in the present study.

**Table 2.** Samples configuration.

| Sample | Base Material 1 (BM2) | Base Material 2 (BM1) | Filler Metal |
|---|---|---|---|
| T9 | Ti6Al4V | KS 1.2 ASN-EX | ER Ti-9 |
| T5 | Ti6Al4V | KS 1.2 ASN-EX | ER Ti-5 |

### *2.2. Welding Procedures*

The welding technique employed in this study for the butt welding of the pipes is GTAW, with the aim of achieving full penetration along the joint center line. Hence, GTAW

was performed with a direct current electrode negative (DCEN) of 35 A, a voltage of 11.8 V coupled with the pure argon gas shielding of 11–13 L/min with a manual travelling speed of approximately 5 mm/s. The tungsten electrode used in the experiment was a 2% thoriated one with a diameter of 1.6 mm, sharpened to 0.8–1 mm tip flat.

### *2.3. Types of Analyses*

The samples welded with different strategies, discussed in Section 2.1were submitted to a complete characterization by tensile testing, Vickers microhardness testing, bend testing, radiographic examination, and penetrant liquid analyses (according to weld qualification standard EN ISO 15614-1 [22]). In addition to that, a complete microstructural examination with optic microscope and scanning electron microscope, as well as a microstructural phases determination by X-ray diffractometry (XRD), has been performed on samples, to better understand the distribution of elements and phases formed.

Radiographic examination and microscopy have been used to determine the dimensions of possible defects in the weld, using image analysis software (ImageJ 1.54a, NIH, USA).

Tensile tests were performed according to UNI EN ISO 6892-1:2020 [23]. The tensile test specimens have been extracted from the welded sample by laser cutting and, as prescribed in UNI EN ISO 4136:2022 standard [24], have been flattened so as to ensure proper gripping between the samples and press clamps. The test specimens were extracted transversely from the welded joint in such a way that, after cutting, the weld axis remains in the middle of the parallel length of the test specimen, as shown in Figure 2.

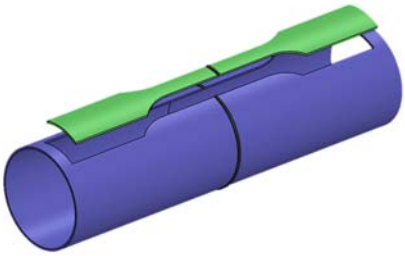

**Figure 2.** Sample extraction.

The resulting specimens, cut out of the cylindrical welded samples, had dimensions of gage length $L_0$ = 50 mm and a cross section of 6 mm × 1 mm. Four tests at room temperature were performed for each welded sample using a hydraulic universal press Galdabini Quasar 50 with maximum load of 50 kN; the mechanical characterization results are presented in terms of average values of such four tests. On the same universal machine, the bend tests were performed as well, using a specific clamping fixture and according to the test method prescribed in UNI EN ISO 5173:2023 standard [25] regarding the root and face method. Samples of 152 mm × 38 mm dimensions, with 1 mm thickness, were used. According to the standard procedure, the weld is parallel to the longitudinal axis of the specimen, which is bent so that the face (for longitudinal face bend) or root (for longitudinal root bend) of the weld surface becomes the convex surface on the bent specimen.

Vickers micro-hardness tests were performed on a Wilson VH 1202 machine, according to UNI EN ISO 6507-1:2018 standard [26] using a load equal to 4905 N, applied for 15 s, and a pyramidal penetrator with 136° angle. The hardness evaluation was made with two different strategies: one is the classical cross section analyses of the full weld joint, creating several indentations along a horizontal line crossing the whole sample from BM to WB areas. The second approach was inspecting just the weld bead creating a grid of microhardness indentations, along the horizontal and vertical testing lines, with the aim of inspecting possible local variations existing across the molten material.

For optical micrographic analysis, samples were mechanically ground using the SiC grinding paper and then polished with colloidal silica (0.04 μm) and hydrogen peroxide

(30%). The Kroll reagent (5 mL $HNO_3$; 10 mL HF; 85 mL $H_2O$) was used as etchant. Samples were then analyzed with a Nikon Eclipse Ci-L optical microscope with fluoride lenses.

Semi-quantitative analysis of the elemental distribution along the welded region was performed using the scanning electron microscopy (ESEM Quanta-200 Fei, Hillsboro, OR, USA) and energy dispersive X-ray spectroscopy (EDS, INCA-350, Oxford Instruments, Abingdon, UK).

The phase compositions of the base materials and the welded zones were determined from X-ray Powder Diffraction (XRPD) collected with a X'Pert PRO multi-purpose diffractometer (PANalytical, Almelo, The Netherlands, Cu-K radiation) working in Bragg–Brentano parafocusing geometry. Data were collected in a linear grid of parallel zones across the welded joint, ranging from one base material to the other. The samples were mounted with the surface of the weld perpendicular to the diffraction vector. The size of the primary beam, and thus the irradiated sample area, was limited by divergence and antiscattering slits (both 1/2° for the base materials; 1/4° and 1/8°, respectively, for the welded zone). Hence, data could selectively be collected from the weld beads and the heat affected zones. The primary beam also included a soller slit (0.04 rad) and a beam mask (7 mm). The diffracted beam passed a Ni filter, a soller slit (0.04 rad), and an antiscatter blade (5 mm) before reaching the Real Time Multiple Strip (RTMS) detector. A virtual step scan (0.0167°/step) was accomplished in the range 30–100°2θ using 50 s/step. The penetration depth of the X-ray beam, calculated using the X'Pert High Score Plus software (PANalytical BV, Almelo, The Netherlands), is approximately 15–26 μm in the investigated 2θ range.

## 3. Results

A preliminary study of possible defects in the welded region ascribable to the use of different fillers has been made, both by radiographic inspection, as shown in Figure 3 and by optical microscopy on cross sections.

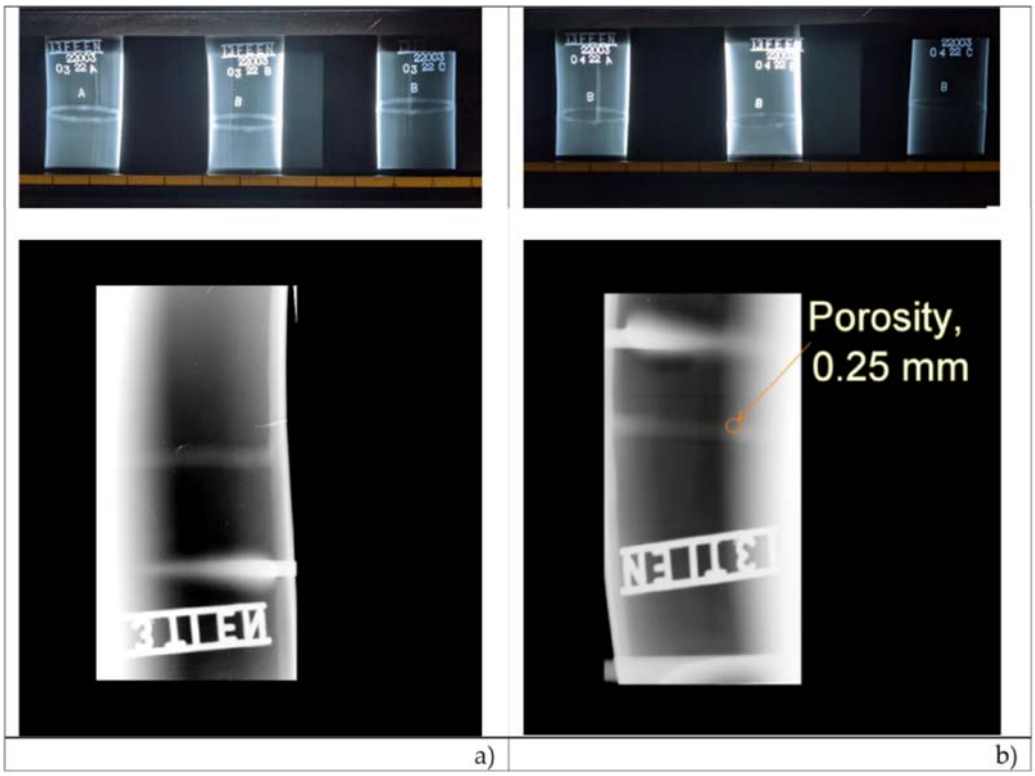


**Figure 3.** Radiographic inspection of: (**a**) T9 and (**b**) T5 joints.

In the case of T5 samples, porosity is found in the WB, while it is almost absent in all the T9 samples observed.

### *3.1. Tensile Test Results*

All the tensile tests performed on the specimens extracted from the welded pipes were always broken on the base material on the side of the less resistant alloy, BM1, which is KS Ti 1.2 ASN-EX.

Table 3 summarizes the results of the tensile tests in terms of offset yield of 0.2% ($Rp_{0.2}$), ultimate tensile strength (UTS), elongation at break (Elong%), and where the break occurred (Break Area).

**Table 3.** Tensile test results—average values of 4 tests.

| Sample | $Rp_{0.2}$ MPa | UTS (MPa) | Elong. (%) | Break Area |
|---|---|---|---|---|
| T9 | 292.0 ± 9.9 | 418.5 ± 10.5 | 11.7 ± 0.3 | BM1 (ASN side) |
| T5 | 302.7 ± 6.9 | 429.7 ± 5.3 | 13.2 ± 0.2 | BM1 (ASN side) |

Results are in agreement with the mechanical properties of the base material, where the fracture occurred, and indicate that both heat affected zone and weld bead present higher tensile properties, as further confirmed by microhardness measurements (see next sections).

### *3.2. Bend Test Results*

Guided bend tests provide a quality control check that helps to determine the ductility of weld metal at the face and root of a welded joint. A guided bend test sample, containing the weld, is located at its center point while being supported by lower anvils. The samples must bend at 180° and then will be visually checked for cracks or defects. No cracks should appear on the surface longer than 3 mm [27]. The outside of the welded bend is plastically deformed so that any defects in, or embrittlement of, the material will be revealed by the premature failure of the coupon. The bend tests performed for this research were performed in accordance with the guided-type method [27], as depicted in Figure 4.

**Figure 4.** Bend test fixture.

Results summarized in Table 4 confirm that the welds' quality was excellent, and the ductility of the BM was still good, as no evidence of defects emerged by the bending tests.

**Table 4.** Bend test results.

| Sample | Specimen | Specimen Orientation | Bending Angle | Test Results |
|---|---|---|---|---|
| T9 | 1 | Root | 180° | No defects |
| | 2 | Root | 180° | No defects |
| | 3 | Face | 180° | No defects |
| | 4 | Face | 180° | No defects |
| T5 | 1 | Root | 180° | No defects |
| | 2 | Root | 180° | No defects |
| | 3 | Face | 180° | No defects |
| | 4 | Face | 180° | No defects |

### *3.3. Micrographic Examinations*

Figure 5 shows the cross section of the specimen T9, welded using ER Ti-9 filler metal, while the one shown in Figure 6 is the specimen T5, welded using ER Ti-5 filler metal.

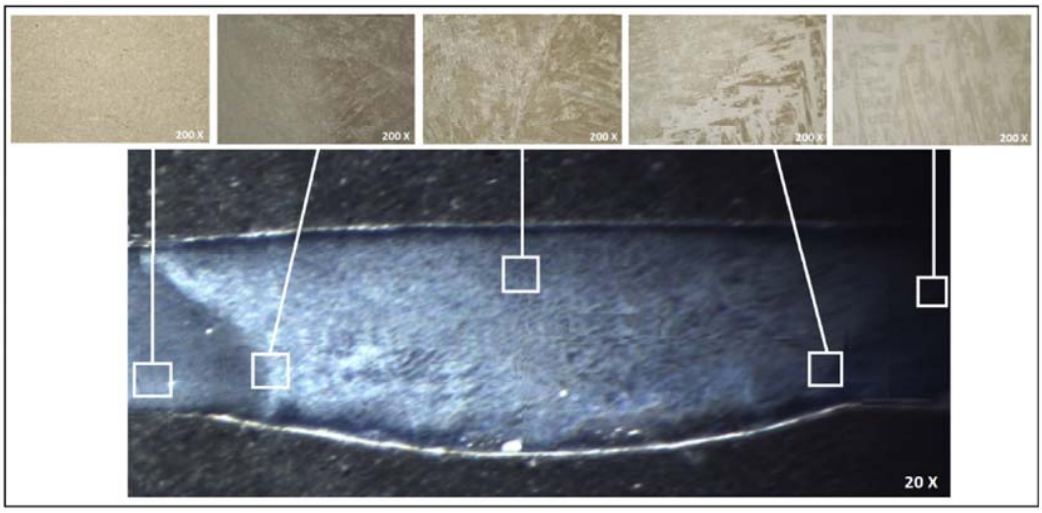


**Figure 5.** Microstructure of T9 sample.

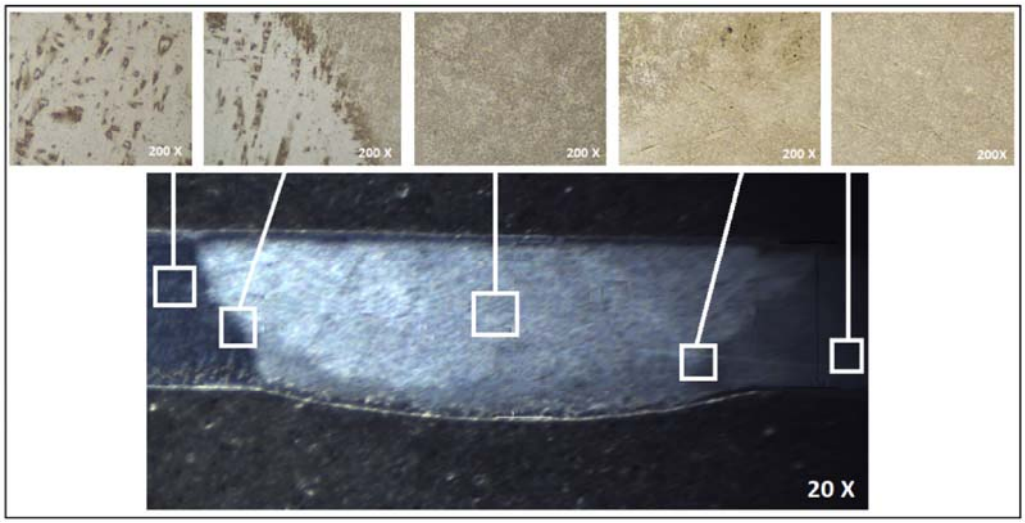


**Figure 6.** Microstructure of T5 sample.

In both specimens, the full penetration bead was obtained and no major defects, such as porosity or misalignment, were observed, as previously confirmed by the radiographic inspections (Figure 3). Based on the difference in microstructure, the joint can be divided into three main zones: base metal (BM), heat affected zone (HAZ), and weld bead (WB), where microhardness measurements have been performed.

In both cases, micrographs show that the WB zone microstructure contains the coarse serrate and acicular α structures of grain boundary α, massive α, and Widmanstätten α + β only in the small portion facing the Ti6Al4V side. The HAZ microstructure on the Ti6Al4V side (right side of Figure 5 and left side of Figure 6) consists of the coarse distorted serrate and acicular α structures of grain boundary α, coarse α + β structure. The HAZ microstructure on the ASN-EX side is practically identical to that of the base material, due to the characteristics of this alloy, developed to withstand high temperatures: As a matter of fact, the minor addition of Al and Si inhibits oxidation of Ti-1.5Al more than in the case of CP titanium and Si is known to form silicide that suppresses grain growth. Hence, the possible uptake of Si in the WB can explain the reason why a not so coarse microstructure is observed in the regions of the WB facing the ASN EX material.

### *3.4. Microhardness Test Results*

#### 3.4.1. Conventional Microhardness Method on Weld Joints

The microhardness measurements were carried out on a transverse section of the weld seam using a semi-automatic microhardness tester. Microhardness profiles were determined by taking indentations with the scheme shown in Figure 7. These profiles were used to identify possible differences in hardness, related to microstructure and chemical composition, existing between base material, HAZ zones, and weld bead.

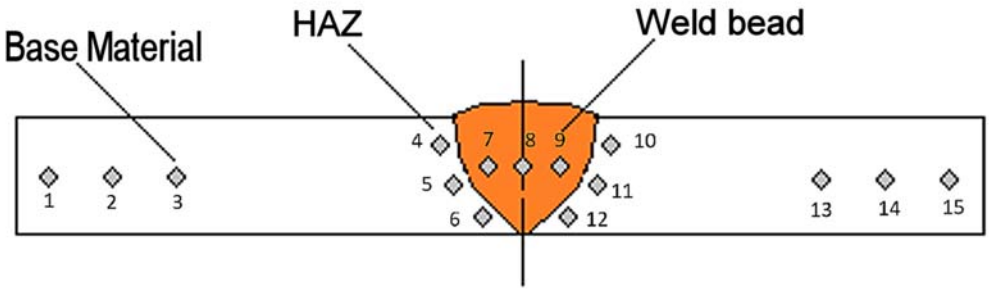


**Figure 7.** Indentation HV0.5 strategy.

The average results of the 15 microhardness measurements are summarized in Figures 8 and 9, with indication of the region of testing.

The results show that, despite the possible assumption of the joint characteristics being dominated by the filler material used, instead, it is mainly the base materials that influence the joint properties, with the ASN material (BM1) being the one presenting lower hardness and the site of fracture during tensile tests.

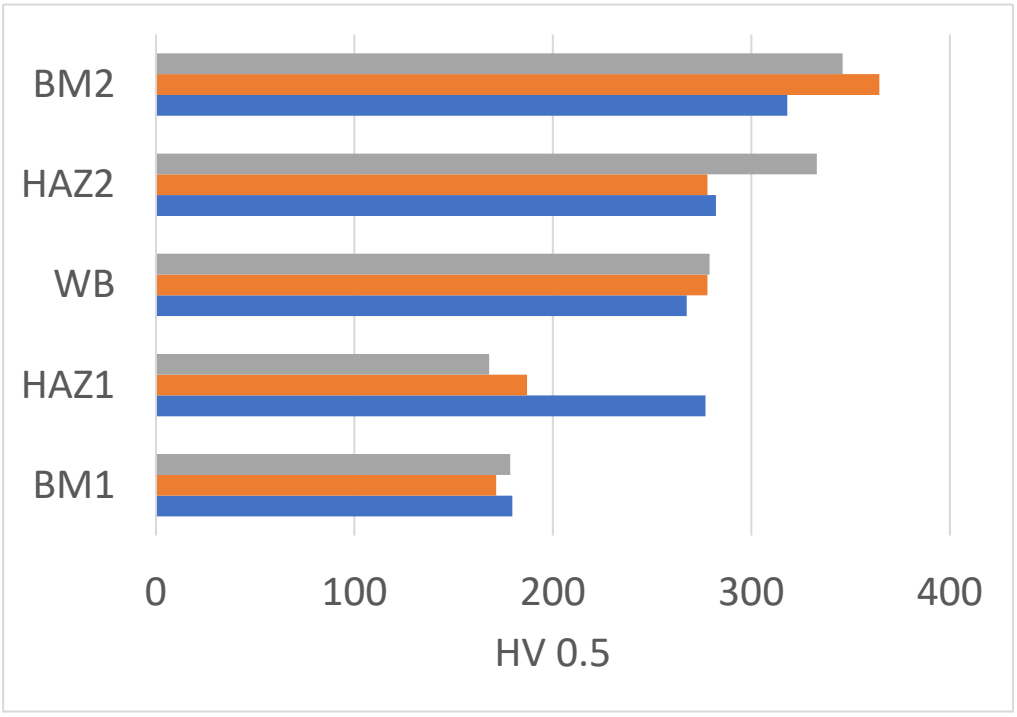


**Figure 8.** HV 0.5 Microhardness values in T9 sample: BM1 = base metal ASN; HAZ1 = Heat Affected Zone of ASN; WB = Weld Bead; HAZ2 = Heat Affected Zone of Ti6Al4V; BM1 = base metal Ti6Al4V.

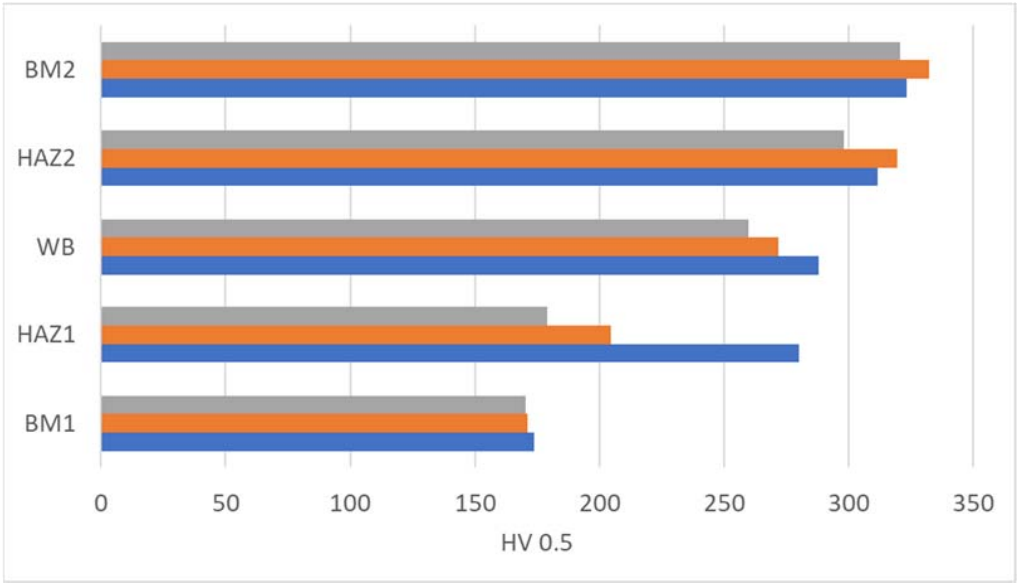


**Figure 9.** Microhardness values in T5 sample: BM1 = base metal ASN; HAZ1 = Heat Affected Zone of ASN; WB = Weld Bead; HAZ2 = Heat Affected Zone of Ti6Al4V; BM1 = base metal Ti6Al4V.

#### 3.4.2. Two-Dimensional Grid Examination

The main focus of this work was investigating how the use of different filler metals used to join dissimilar titanium alloys affects the weld bead microstructure and alloying elements distribution. To explore this further, a series of Vickers micro-hardness measurements were taken creating a two-dimensional grid with a 0.2 mm spacing covering the whole fused zone, as indicated in Figure 10, using a 100 g load and 10 s dwell time.

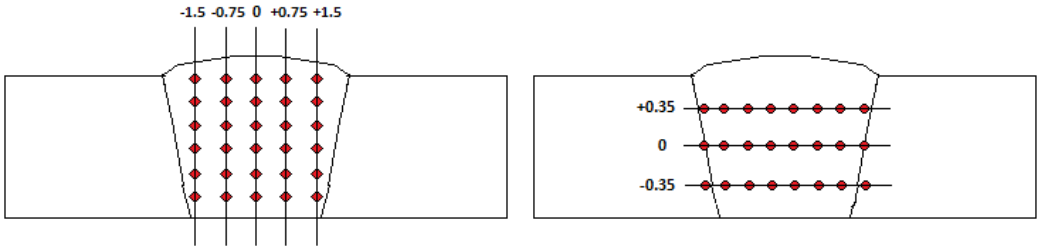


**Figure 10.** Indentation map positions along vertical and horizontal lines.

Results of the vertical mapping are plotted in Figure 11, providing a micro-hardness map of the WB region, while the profiles of the horizontal mapping are shown in Figure 12.

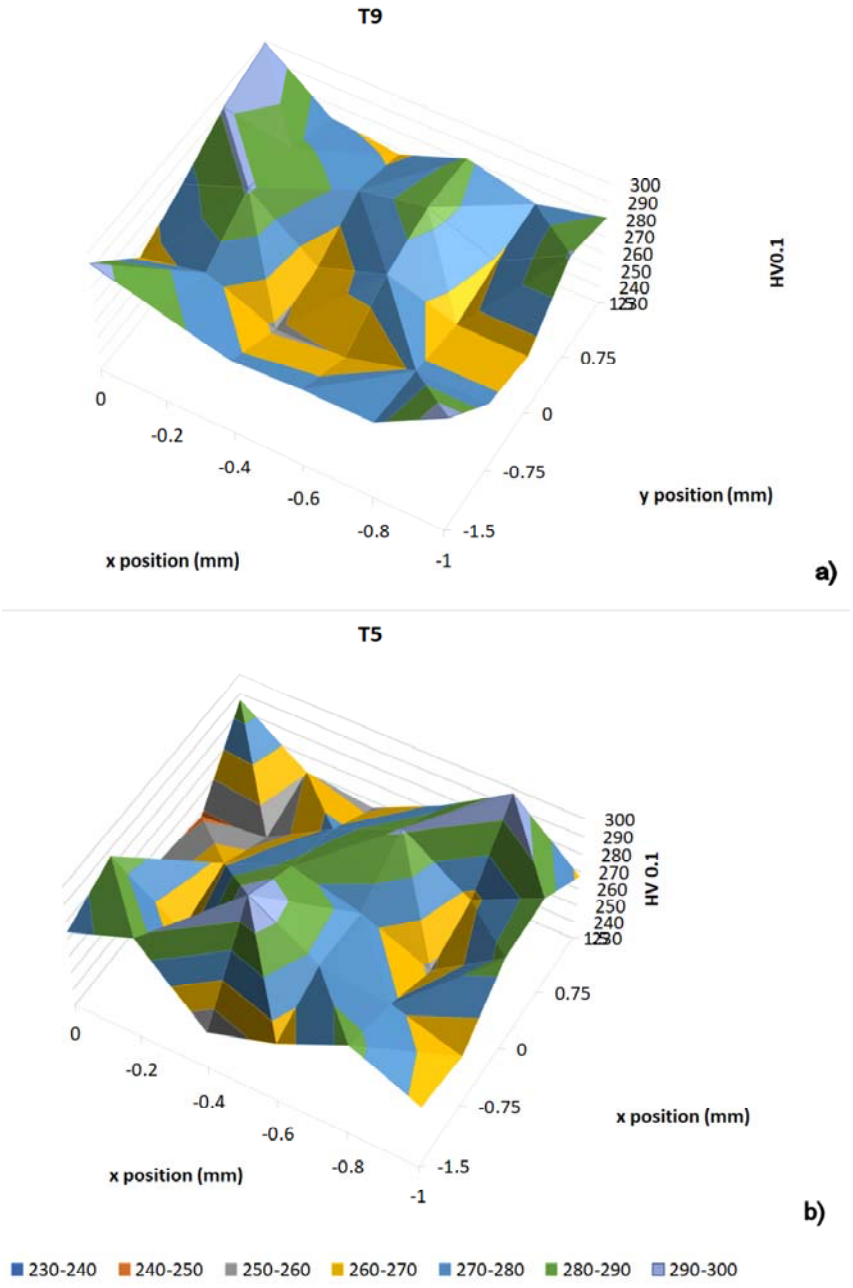


**Figure 11.** HV 0.1 indentation map of WB in sample (**a**) T9 and (**b**) T5.

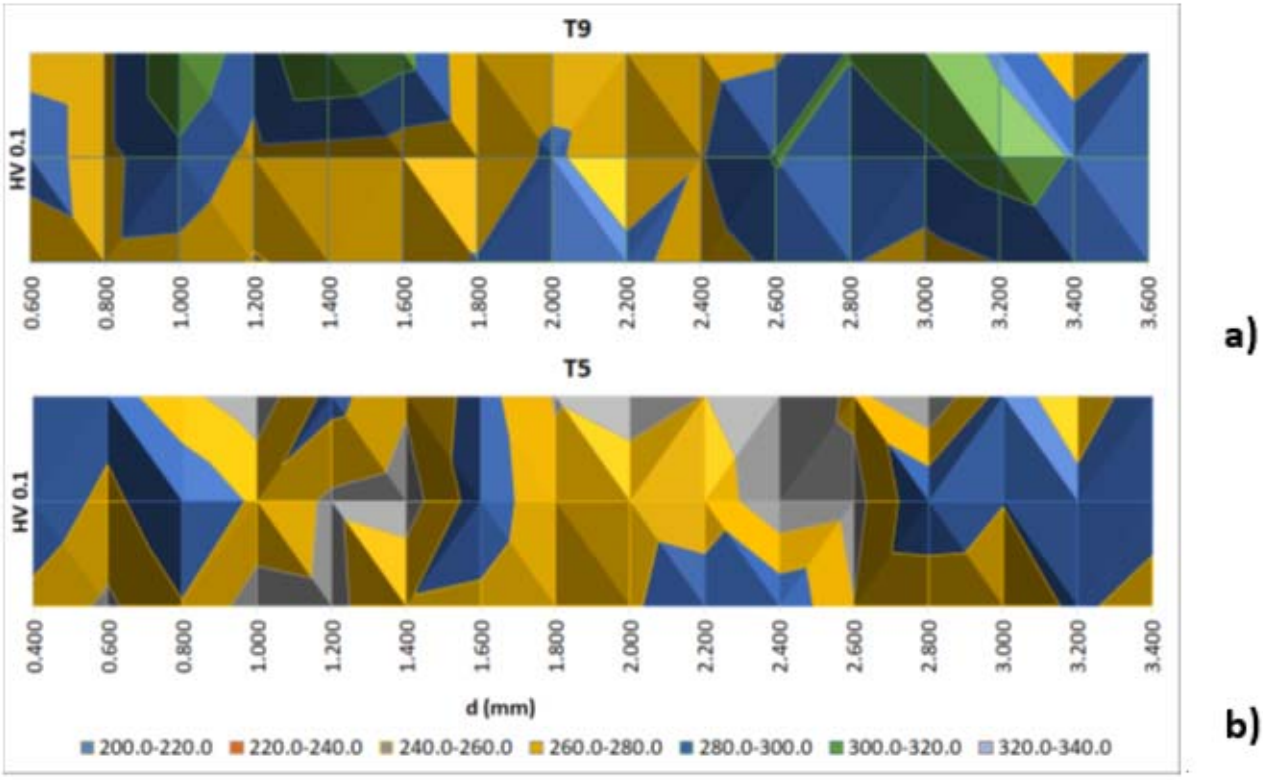


**Figure 12.** HV 0.1 indentation maps of WB in sample (**a**) T9 and (**b**) T5.

Results demonstrate the existence of a pronounced variation of microhardness values in the WB, due the local differences in microstructure and possibly, as demonstrated in next section, in chemical composition.

### *3.5. EDS Profiles*

The EDS, along with SEM, is typically used for elemental composition surveys. This technique is mostly used for qualitative analysis of materials, but is capable of providing semi-quantitative results as well. In our specific case, the EDS examination was conducted with the primary intention of investigating the change in the dilution of alloying elements in the weld bead, possibly finding a correlation between the local chemical composition and microhardness profile, specifically in the weld beads. For this reason, the EDS analysis has been performed close to the microhardness indentations.

The results of the EDS line scan, performed on a horizontal center line of the welds section, at minimum spatial resolution of 0.15 mm per step, are presented in Figure 13.

As expected, the higher alloying element content in samples T5 is responsible for a higher Al and V content in the fused zone, progressively decreasing when moving from the grade 5 base material (BM2) to the ASN one (BM1). Similarly, Si, originally present only in the ASN material, presents an increasing content when moving from the grade 5 alloy towards the ASN one.

Hence, considering the mechanical properties measured, the use of a filler material, similar to the base material Ti6Al4V, results show that the aluminum content in the WB is, on average, equal to 3.91%, vanadium 2.48%, and an average micro hardness of 278.4 HV0.1. When using a filler with lower amount of the alloying elements, the WB composition is not changing proportionally, presenting 3.35% aluminum, vanadium 2.12%, and an average hardness of 264.6 HV0.1. It is worth remembering that the resulting mechanical properties, measured by tensile testing, are slightly lower for the T9 sample, but similar (in both cases the fracture occurs on the ASN side).

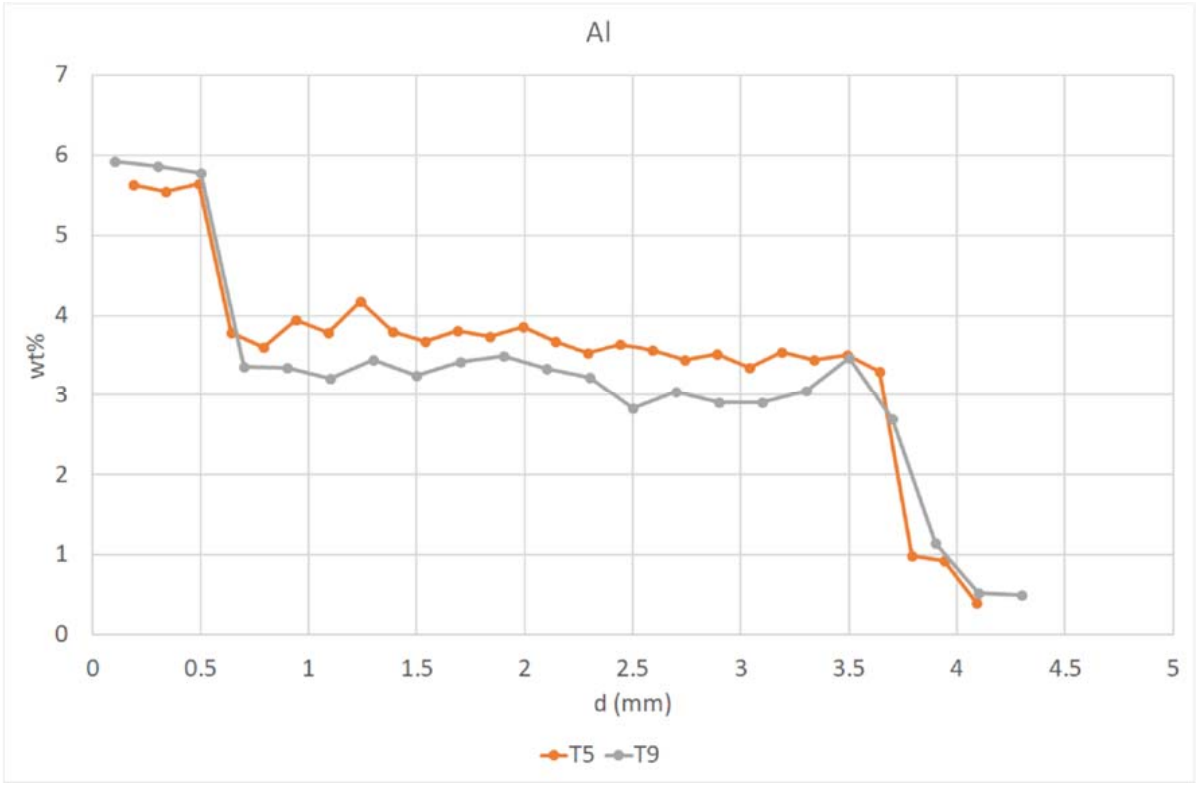


(**a**)

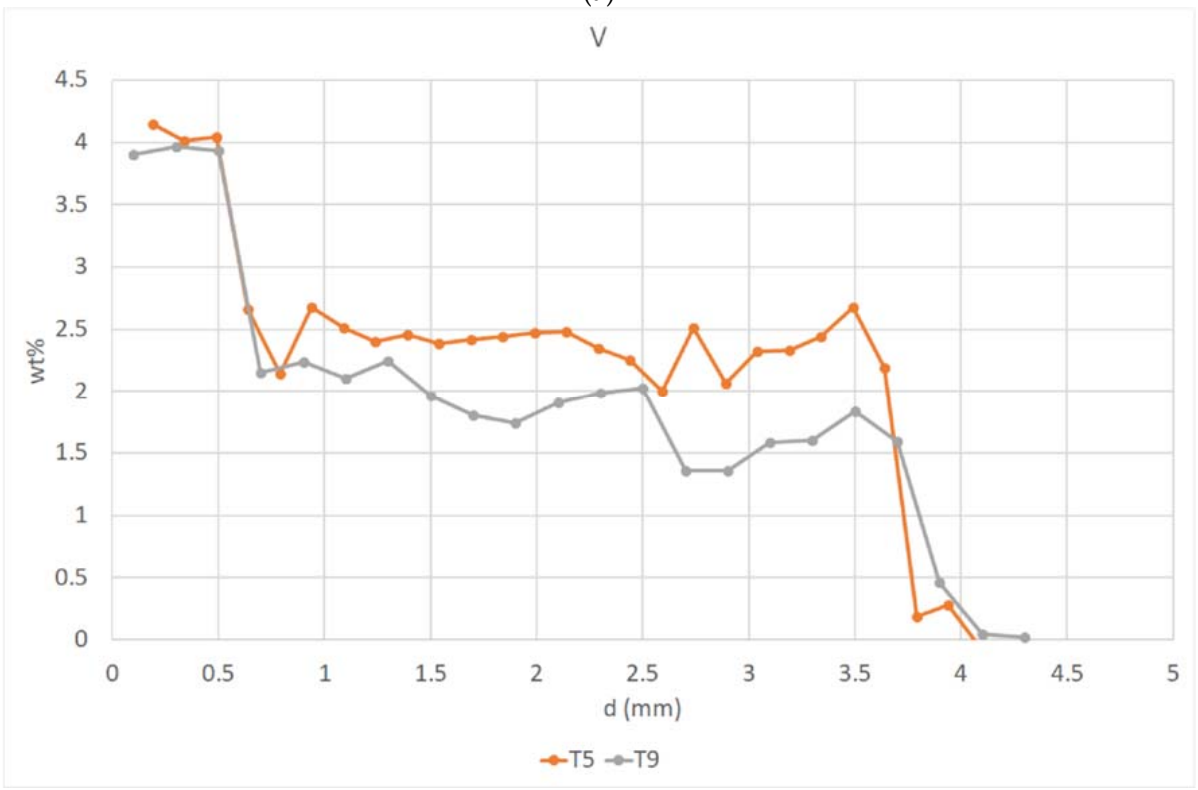


(**b**)

**Figure 13.** *Cont*.

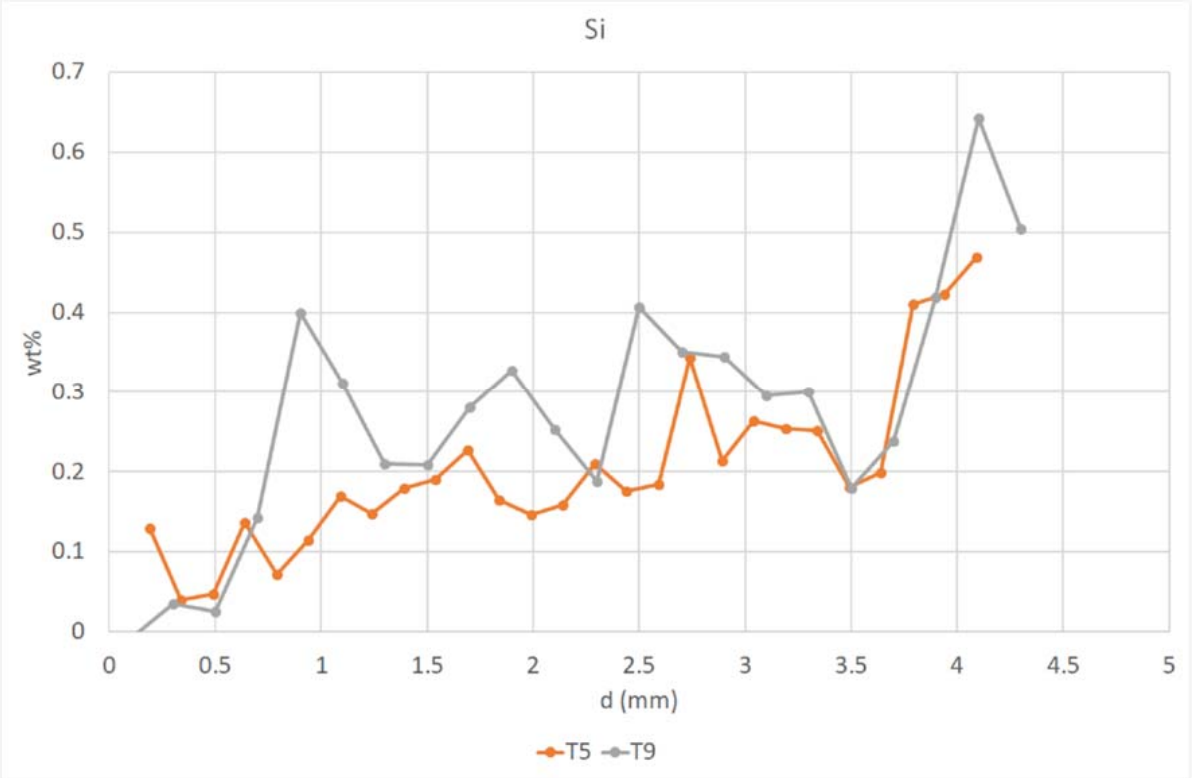


(**c**)

**Figure 13.** Element maps of (**a**) Al, (**b**) V, and (**c**) Si along the central horizontal line of the WB: Grade 5 side on the left, ASN side on the right.

### *3.6. XRD Analysis*

To evidence the possible differences between the two filler materials, XRD on the WB has been used. Figures 14 and 15 show the XRD data collected from the base materials and from the weld zones, respectively.

First of all, the phase compositions in the two base materials confirm the nominal ones, expected from the material supplied. In fact, the Ti6Al4V alloy is mainly composed of the alpha-phase (JCPDF file 44-1294, space group P63/mmc) in addition to a minor quantity of the beta-phase (JCPDF 44-1288, Im-3m). Instead, the Ti-KS 1.2ASN-EX alloy is composed of pure alpha-phase. The XRD data were also collected from the various areas of the welded zone of both investigated samples, only differing in the filler metal used (ER Ti-9 for T9 and ER Ti-5 for T5). All diffractograms show reflections of the α-phase (JCPDF 44-1294), whereas the β-phase could only be detected in the heat affected zone (HAZ) on the Ti6Al4V side when ER Ti-5, having the same composition as the Ti6Al4V base material, was used as filler metal (sample T5).

The XRD patterns were used to evaluate the c/a ratio of alpha or metastable alpha prime phases (distinguishing between these two phases by XRD patterns collected in the experimental conditions used in this study is challenging, as both are characterized by the same hexagonal structure [28]), as shown in Table 5.

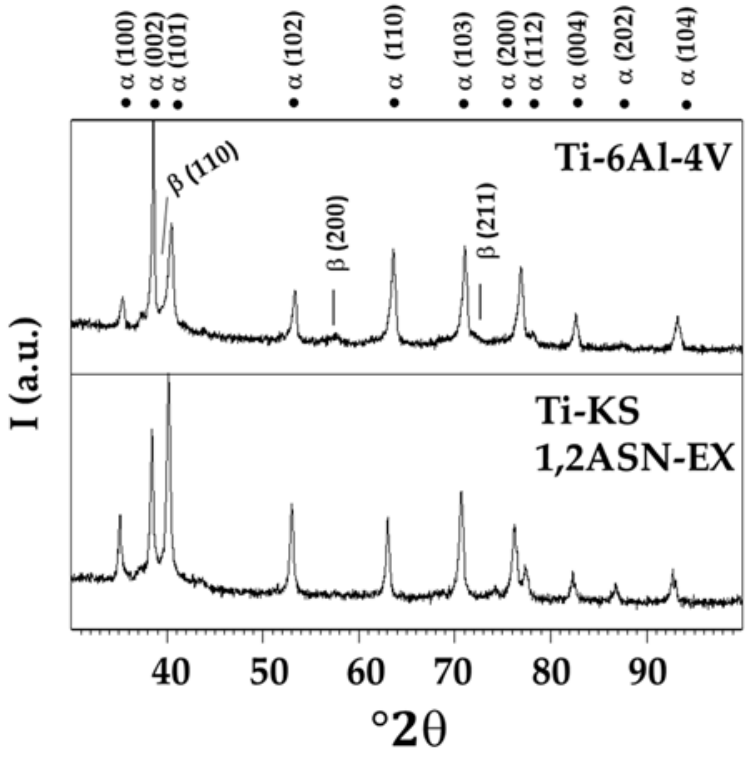


**Figure 14.** XRD data collected from the base materials Ti6Al4V (alpha/beta-type alloy) and Ti-Ks 1.2ANS-Ex. (alpha-type alloy). Reflections of the α-phase (hcp) and the β-phase (cubic) are indexed according to JCPDF 44-1294 and 44-1288, respectively.

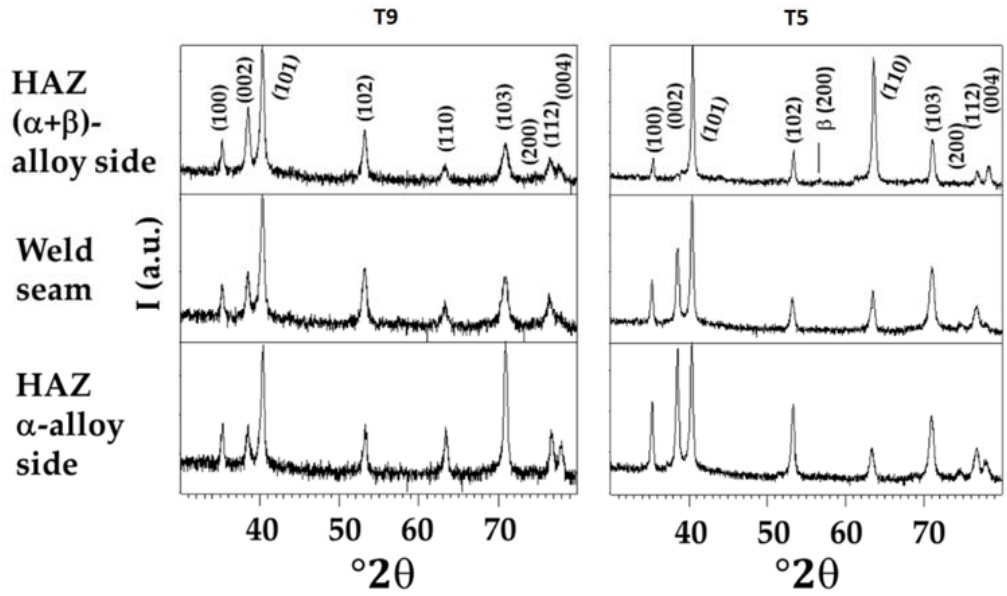


**Figure 15.** XRD data collected from different areas of the weld zone: heat affected zone on the Ti6Al4V side (HAZ (α + β)-alloy); weld seam; heat affected zone on the Ti-KS 1.2ASN-EX side (HAZ α-alloy). The patterns show reflections of the α-phase (hcp), indexed according to JCPDF 44-1294. Weak reflections of the β-phase are only observed in the HAZ on the Ti6Al4V side in sample PQR_21 where the filler material was ER Ti-5 having the same composition as the Ti6Al4V base material (β-phase indexed according to JCPDF 44-1288).

**Table 5.** The c/a ratio of the alpha or alpha prime phases.

| Position | c/a Ratio |
|---|---|
| Ti6Al4V | 1.59306 ± 0.00042 |
| Ti-KS 1,2 ASN-Ex | 1.58693 ± 0.00021 |
| T9-weld bead | 1.59175 ± 0.00058 |
| T9_HAZ grade 5 side | 1.59057 ± 0.00049 |
| T9_HAZ_ASN side | 1.59261 ± 0.00052 |
| T5-weld bead | 1.59089 ± 0.00037 |
| T5_HAZ grade 5 side | 1.59777 ± 0.00047 |
| T5_HAZ_ASN side | 1.59087 ± 0.00044 |

Errors reported for the a/c ratio in the last column of Table 5 were obtained from the error of the refined unit cell and subsequent error propagation calculations. These are, thus, errors calculated based on pattern fitting and not on variations within the sample. Nevertheless, results are consistent with the typical values of Ti6Al4V alloys from literature [29]. Rather interestingly, they show that in the WB zone, the c/a ratio tends to be lower than in the parent material. The smaller values of the c/a ratio indicate the presence of martensite, possibly supersaturated with β stabilizing elements, which tend to distort the lattice [30]. Such martensite (alpha prime phase) formation can be ascribed to the rapid cooling from the molten state, after the weld pass. The fact that low c/a ratios are also found in the HAZ can be ascribed to the slightly overlapping of the WB region with the HAZ during X-ray collection, despite the experimental setup used to achieve as localized values as possible.

### *3.7. General Discussion*

Based on the experimental results obtained, the substantial equivalence of the two filler materials can be explained as follows: in the case of rapid heating, e.g., during the welding, the transformation of phase α to phase ß does not follow the equilibrium diagram. According to literature results, dissolution of the α phase occurs at a higher temperature, when applying the high heating rates [31]. When rapidly cooling from the field of the ß phase, there is a martensitic transformation, which has an acicular appearance with small needles at the optical microscope observation. Moreover, it presents distorted c/a ratio in XRD patterns.

Superimposing the microhardness profiles and the semi-quantitative EDS analysis results for the WB (Figure 16), it is evident that there is one major difference between the two sets of samples, i.e., a different gradient of the V/Al ratio. This is a rather expected trend, due to the fact that in the case of T5 samples, the filler material is practically identical to the grade 5 base material on one side of the joint, while in the case of T9 filler, this does not occur.

The plots of Figure 16 also show similar trends for the variation of microhardness related to the V/Al ratio. A quantitative trend cannot be determined easily, due to the slightly different positions of the microindentations (horizontal line at 0 mm, with reference to Figure 10) and EDS analysis site (shifted of approximately 0.05 mm along the vertical direction).

Nevertheless, regions with higher V/Al ratio tend to present slightly higher microhardness values. This could be explained considering the high cooling rate experienced by the WB. It can be assumed that the higher the V/Al ratio, the higher the tendency to form supersaturated alpha or alpha prime phases upon solidification and cooling and hence to present a higher hardness value with respect to the regions with the lower V/Al ratio.

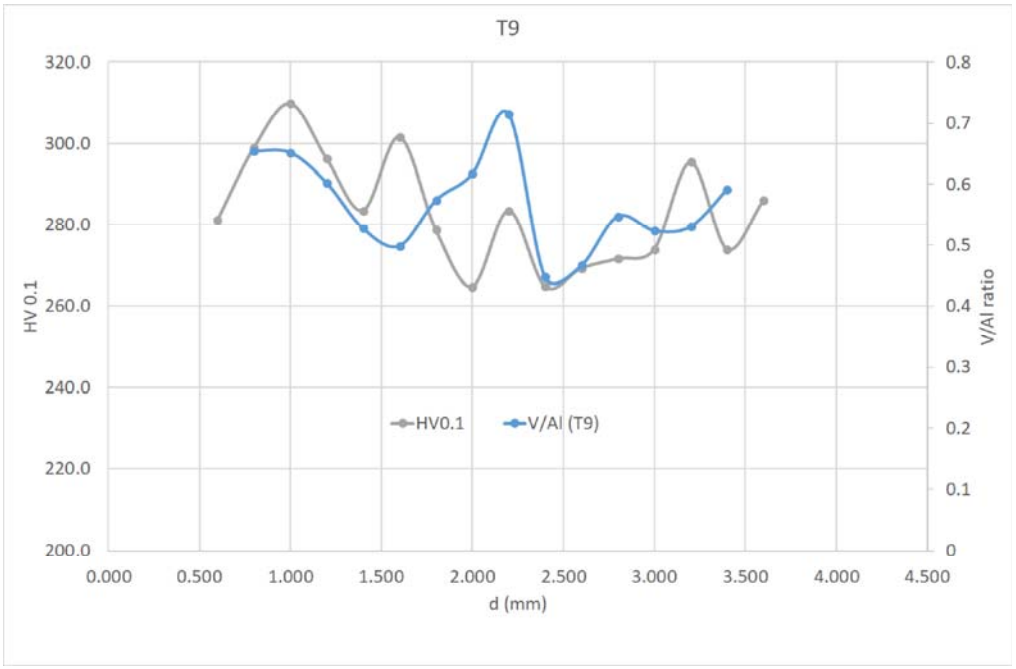


(**a**)

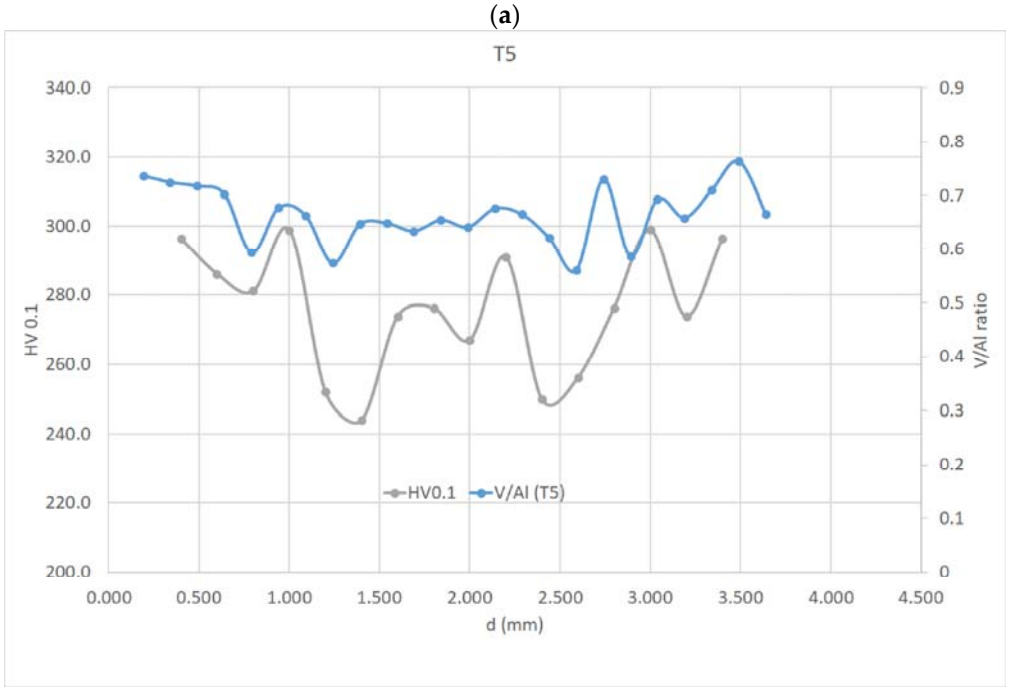


(**b**)

**Figure 16.** V/Al ratio and measured HV0.1 profiles in the case of (**a**) T5 and (**b**) T9 samples: Grade 5 side on the left and ASN side on the right.

## 4. Conclusions

The main objective of this work was to determine which filler material is most effective and performs best for making a weld joint on titanium alloys belonging to both dissimilar and homogeneous families.

Upon analyzing the samples under study, it was found that the filler materials investigated, despite a significantly different chemical composition, only marginally affected the mechanical and chemical composition characteristics of the joint. The generally higher alloying element content of T5 samples was responsible for different compositional gradients existing when moving from one base material to the other, but it had minor effects

on tensile testing results, dominated by the fracture occurring in the ASN base material, and on microhardness profiles. A possible correlation of microhardness from the V/Al ratio, determined by EDS measurements, emerged, but further investigations are required to confirm this trend. Possible formation of substitutional elements-enriched alpha prime phases has been confirmed by XRD, evidenced by smaller c/a ratios of the alpha phases in the WB. Last but not least, radiographic analysis also made it possible to observe that joints made with ER Ti-9 material tend to be less prone to generate porosity in the experimental conditions tested. The ER Ti-9 filler material was also more flowable during the welding, making its adoption preferable to ER Ti-5 wire.

**Author Contributions:** Conceptualization, S.G. and P.V.; Methodology, S.G.; Software, M.G.; Formal analysis, S.G., M.G., E.F., A.M., M.L.G. and E.C.; Investigation, M.G., E.F., A.M., M.L.G. and E.C.; Resources, S.G.; Data curation, M.G., E.F., M.L.G. and E.C.; Writing—original draft, S.G., M.L.G. and P.V.; Writing—review & editing, M.G. and E.F.; Supervision, P.V.; Project administration, E.F. All authors have read and agreed to the published version of the manuscript.

**Funding:** This research received no external funding.

**Data Availability Statement:** The data presented in this study are available on request from the corresponding authors. The data are not publicly available due to their confidential nature.

**Conflicts of Interest:** The authors declare no conflict of interest.

## References

1. Blanch, O.L.; Pope, J.; Violatos, I.; Rahimi, S.; Jackson, M. Residual Stress Distributions in Dissimilar Titanium Alloy Diffusion Bonds Produced from Powder Using Field-Assisted Sintering Technology (FAST-DB). *Met. Mater. Trans. A* **2023**, *54*, 3578–3593. [CrossRef]
2. Rae, W.; Lomas, Z.; Jackson, M.; Rahimi, S. Measurements of residual stress and microstructural evolution in electron beam welded Ti-6Al-4V using multiple techniques. *Mater. Charact.* **2017**, *132*, 10–19. [CrossRef]
3. McAndrew, A.R.; Colegrove, P.A.; Bühr, C.; Flipo, B.C.; Vairis, A. A literature review of Ti-6Al-4V linear friction welding. *Prog. Mater. Sci.* **2018**, *92*, 225–257. [CrossRef]
4. Rajan, S.; Wanjara, P.; Gholipour, J.; Kabir, A.S. Joining of Dissimilar Alloys Ti-6Al-4V and Ti-6Al-2Sn-4Zr-2Mo-0.1Si Using Linear Friction Welding. *Materials* **2020**, *13*, 3664. [CrossRef] [PubMed]
5. Esmaily, M.; Nooshin Mortazavi, S.; Todehfalah, P.; Rashidi, M. Microstructural characterization and formation of $\alpha'$martensite phase in Ti–6Al–4V alloy butt joints produced by friction stir and gas tungsten arc welding processes. *Mater. Des.* **2013**, *47*, 143–150. [CrossRef]
6. Braga, D.F.; Eslami, S.; Moreira, P. Friction Stir Welding. In *Advanced Joining Processes*; Elsevier: Amsterdam, The Netherlands, 2021; pp. 173–206. [CrossRef]
7. Medvedev, A.; Mendes, A.; Lapovok, R.; Semiatin, S. Shear-induced, solid-state joining of Ti-6Al-4V and Ti17 titanium alloys. *Mater. Sci. Eng. A* **2018**, *737*, 253–264. [CrossRef]
8. Du, S.; Liu, H.; Gao, Y.; Hu, Y.; Zhou, L. Effects of process parameters on joint formation and tool wear behavior in friction stir welded TA5 alloy. *Int. J. Adv. Manuf. Technol.* **2022**, *123*, 2531–2547. [CrossRef]
9. Amirov, A.; Chumaevskii, A.; Savchenko, N.; Gurianov, D.; Nikolaeva, A.; Krasnoveykin, V.; Ivanov, A.; Rubtsov, V.; Kolubaev, E. Features of Permanent Joints of Titanium ($\alpha + \beta$)-Alloys Obtained by Friction Stir Welding Using a Nickel Superalloy Tool. *Metals* **2023**, *13*, 222. [CrossRef]
10. Tarasov, S.; Amirov, A.; Chumaevskiy, A.; Savchenko, N.; Rubtsov, V.E.; Ivanov, A.; Moskvichev, E.; Kolubaev, E. Friction Stir Welding of Ti-6Al-4V Using a Liquid-Cooled Nickel Superalloy Tool. *Technologies* **2022**, *10*, 118. [CrossRef]
11. Chumaevskii, A.; Amirov, A.; Ivanov, A.; Rubtsov, V.; Kolubaev, E. Friction Stir Welding/Processing of Various Metals with Working Tools of Different Materials and Its Peculiarities for Titanium Alloys: A Review. *Metals* **2023**, *13*, 970. [CrossRef]
12. Li, L.; Sun, L.; Li, M. Diffusion bonding of dissimilar titanium alloys via surface nanocrystallization treatment. *J. Mater. Res. Technol.* **2022**, *17*, 1274–1288. [CrossRef]
13. Pope, J.J.; Calvert, E.L.; Weston, N.S.; Jackson, M. FAST-DB: A novel solid-state approach for diffusion bonding dissimilar titanium alloy powders for next generation critical components. *J. Mater. Process. Technol.* **2019**, *269*, 200–207. [CrossRef]
14. Gietzelt, T.; Toth, V.; Huell, A. *Joining Technologies*; IntechOpen: London, UK, 2016; Chapter 9; pp. 195–216. [CrossRef]
15. Farrokhi, A. Welding Properties of Titanium Alloys Grade 5. In *Titanium Alloys—Recent Progress in Design, Processing, Characterization, and Applications*; IntechOpen: London, UK, 2023. [CrossRef]
16. Veronesi, P.; Balestri, A.; Colombini, E. Improvement in Wear Resistance of Grade 37 Titanium by Microwave Plasma Oxy-Carburizing. *Technologies* **2023**, *11*, 13. [CrossRef]
17. Raja, V.B.; Palanikumar, K.; Kannan, S.; Sonawwanay, P.D.; Sahas, S.; Muralidharan, S. Influence of welding parameters on mechanical and corrosion properties of Ti6Al4V alloy. *Mater. Today Proc.* **2023**. [CrossRef]

18. Mehdi, B.; Badji, R.; Ji, V.; Allili, B.; Bradai, D.; Deschaux-Beaume, F.; Soulié, F. Microstructure and residual stresses in Ti-6Al-4V alloy pulsed and unpulsed TIG welds. *J. Mater. Process. Technol.* **2016**, *231*, 441–448. [CrossRef]
19. Sundaresan, S.; Ram, G.J.; Reddy, G.M. Microstructural refinement of weld fusion zones in $\alpha$–$\beta$ titanium alloys using pulsed current welding. *Mater. Sci. Eng. A* **1999**, *262*, 88–100. [CrossRef]
20. Mi, G.; Wei, Y.; Zhan, X.; Gu, C.; Yu, F. A coupled thermal and metallurgical model for welding simulation of Ti–6Al–4V alloy. *J. Mater. Process. Technol.* **2014**, *214*, 2434–2443. [CrossRef]
21. American Welding Society (AWS). *Specification for Titanium and Titanium-Alloy Welding Electrodes and Rods*, 6th ed.; American Welding Society: Doral, FL, USA, 2013.
22. *ISO 15614-1:2017*; Specification and Qualification of Welding Procedures for Metallic Materials–Welding Procedure Test—Part 1: Arc and Gas Welding of Steels and Arc Welding of Nickel and Nickel Alloys. International Organization for Standardization: Geneva, Switzerland, 2022.
23. *ISO 6892-1:2020*; Metallic Materials—Tensile Testing–Part 1: Method of Test at Room Temperature. International Organization for Standardization: Geneva, Switzerland, 2020.
24. *ISO 4136:2022*; Destructive Tests on Welds in Metallic Materials—Transverse Tensile Test. International Organization for Standardization: Geneva, Switzerland, 2022.
25. *ISO 5173:2023*; Destructive Tests on Welds in Metallic Materials—Bend Tests. International Organization for Standardization: Geneva, Switzerland, 2023.
26. *ISO 6507-1:2018*; Metallic Materials—Vickers Hardness Test—Part 1–4: Test Method. International Organization for Standardization: Geneva, Switzerland, 2018.
27. *ASTM E190-21*; Standard Test Method for Guided Bend Test for Ductility of Welds. ASTM International: West Conshohocken, PA, USA, 2021.
28. Wysocki, B.; Maj, P.; Sitek, R.; Buhagiar, J.; Kurzydłowski, K.J.; Święszkowski, W. Laser and electron beam additive manufacturing methods of fabricating titanium bone implants. *Appl. Sci.* **2017**, *7*, 657. [CrossRef]
29. Oh, J.-M.; Lee, B.-G.; Cho, S.-W.; Lee, S.-W.; Choi, G.-S.; Lim, J.-W. Oxygen effects on the mechanical properties and lattice strain of Ti and Ti-6Al-4V. *Met. Mater. Int.* **2011**, *17*, 733–736. [CrossRef]
30. Cho, J. Characterization of the $\alpha'$-Martensite Phase and Its Decomposition in Ti-6Al-4V Additively Manufactured by Se-lective Laser Melting. Ph.D. Thesis, RMIT University, Melbourne, Australia, 2018.
31. Charles, C. Microstructure Model for Ti-6Al-4V used in Simulation of Additive Manufacturing. Ph.D. Thesis, Lulea University of Technology, Lulea, Sweden, 2016.